Bioactive Materials 30 (2023) 184–199

Contents lists available at ScienceDirect

Bioactive Materials

journal homepage: www.keaipublishing.com/en/journals/bioactive-materials

Perfusability and immunogenicity of implantable pre-vascularized tissues recapitulating features of native capillary network

Dhavan Sharma [a], Archita Sharma [a], Linghao Hu [a], Te-An Chen [a], Sarah Voon [a], Kayla J. Bayless [b], Jeremy Goldman [c], Alex J. Walsh [a], Feng Zhao [a,*]

[a] Department of Biomedical Engineering, Texas A&M University, College Station, TX, United States
[b] School of Medicine, Texas A&M University, College Station, TX, United States
[c] Department of Biomedical Engineering, Michigan Technological University, Houghton, MI, United States

ARTICLE INFO

Keywords:
Pre-vascularization
Micro-vasculature
Mesenchymal stem cells
Extracellular matrix
Fluorescence lifetime imaging

ABSTRACT

Vascularization is a key pre-requisite to engineered anatomical scale three dimensional (3-D) constructs to ensure their nutrient and oxygen supply upon implantation. Presently, engineered pre-vascularized 3-D tissues are limited to only micro-scale hydrogels, which meet neither the anatomical scale needs nor the complexity of natural extracellular matrix (ECM) environments. Anatomical scale perfusable constructs are critically needed for translational applications. To overcome this challenge, we previously developed pre-vascularized ECM sheets with long and oriented dense microvascular networks. The present study further evaluated the patency, perfusability and innate immune response toward these pre-vascularized constructs. Macrophage-co-cultured pre-vascularized constructs were evaluated *in vitro* to confirm micro-vessel patency and perturbations in macrophage metabolism. Subcutaneously implanted pre-vascularized constructs remained viable and formed a functional anastomosis with host vasculature within 3 days of implantation. This completely biological pre-vascularized construct holds great potential as a building block to engineer perfusable anatomical scale tissues.

1. Introduction

Recent progress in the field of regenerative medicine has advanced the fabrication of tissue analogues to replace damaged or diseased tissues, and for disease modelling. One of the long-standing challenges in current approaches is the limited size of engineered tissues, restricted to up to a few hundred microns in thickness due to the lack of anatomical scale built-in microvasculature [1]. As for millimeter-scale or larger three-dimensional (3-D) tissue constructs, the spontaneous growth of host micro-vessels toward the implants occurs at the rate of several tenths of microns per day [2]. At this rate, the complete vascularization of an implant sizing several millimeters will require several weeks or months depending on the implant site and biomaterials involved [2]. Hence, a built-in and dense microvasculature with anastomotic capability, which enables nutrient and oxygen supply, is crucial to engineered 3-D tissue analogues or constructs to ensure their survival and regenerative potential post transplantation. To address this challenge, advanced micro-scaffolding, surface-patterning, and 3-D printing techniques have designed and fabricated vascular network with diameters of several tens of microns and above [3–5]. Although these approaches are promising for disease modelling and drug screening, the micro-vessels generated by these strategies are oversized and/or not sufficiently dense compared with native vasculatures, and are therefore not able to ensure the survival of implanted organoids or tissue constructs [3]. Advanced microfluidics-based approaches have emerged to fabricate microvascular self-assemblies inside an ECM-mimicking hydrogel that is surrounded by two large vessels in a microdevice [6–8]. Although perfusion was successfully achieved in the micro-vessels, the microscale of the engineered tissues has limited their applications to *in vitro* platforms for disease modeling and drug screening [6–8]. Moreover, the patency, perfusion and immunogenicity of these self-assembled vasculature has not been validated *in vivo*. Presently, anatomical scale perfusable constructs are critically needed for translational applications. Rapid anastomosis of the engineered microvasculature with host vessels must also occur to ensure the perfusion and functional performance of the pre-vascularized constructs

Peer review under responsibility of KeAi Communications Co., Ltd.
* Corresponding author. Department of Biomedical Engineering, Texas A&M University,United States.
E-mail address: fengzhao@tamu.edu (F. Zhao).

https://doi.org/10.1016/j.bioactmat.2023.07.023
Received 21 March 2023; Received in revised form 26 July 2023; Accepted 27 July 2023

post implantation [9].

Advanced microscopy and high-resolution imaging techniques have revealed that most native tissues including skin [10], cardiac [11,12] and skeletal muscle [13] have microvasculature and ECM components organized in a precise architecture to achieve maximal function. To attain such a microvasculature, we previously developed a physiological angiogenesis-mimicking approach in which human endothelial cells (ECs) self-assembled into a microvascular network, with the support of human mesenchymal stem cell (hMSCs), under precisely controlled oxygen concentrations [14,15]. hMSCs were adopted as a bulk cell in the system because they have been recognized for their strong immunomodulatory and regenerative properties via paracrine mechanisms that include secretion of cytokines, growth factors, exosomes and microvesicles [16]. Additionally, an excellent immunomodulatory and safety profile of allogenic hMSCs have enabled their infusion in human clinical trials for the treatment of autoimmune and severe viral diseases, with over 10,000 patients during the past two decades [17,18]. These superior properties have identified hMSCs as an ideal cell type in diverse tissue engineering applications and interventions. To guide the organization of hMSCs, we have created a highly aligned nanofibrous extracellular matrix (ECM) scaffold [19], which is robust and large, with an area up to 25 cm^2, allowing us to engineer a transplantable hMSC/ECM sheet with tunable structures, independent of any external dynamic culture system. By further seeding ECs, highly dense and mature microvasculature with the same order of magnitude as native capillaries were formed on the hMSC/ECM sheet [14,20], which can be utilized as building blocks to engineer 3D pre-vascularized tissue constructs by layering the pre-vascularized cell sheets or integrating the pre-vascularized cell sheets into the engineered 3D constructs. Besides directly promoting tissue regeneration after implantation, hMSCs also act as perivascular cells that support and mature the newly assembled micro-vessels on the pre-vascularized hDF-ECM sheet [17,21,22]. However, one of the major concerns related to static-culture self--assembled micro-vessels, which have a diameter <20 μm, is their patency and perfusability *in vitro* and *in vivo*. In addition, the immunogenicity of pre-vascularized constructs must be evaluated to ensure their long-term survival and functionality post implantation.

Herein, the objective of the current work was to evaluate immune-compatibility, patency, and anastomotic capability of the structured microvascular networks self-assembled on hDF-ECM scaffolds. Immunogenicity of the engineered pre-vascularized construct was evaluated via *in vitro* characterization of macrophage response to the constructs by label-free fluorescence lifetime imaging (FLIM) along with cytokine release profile and regulatory metabolic protein expression. Finally, anastomotic ability, perfusability and immunogenicity of the engineered pre-vascularized tissues were evaluated *in vivo* via subcutaneous implantation in athymic nude rats, which have a robust innate immune system and have been well-accepted to evaluate tissue-implants *in vivo* [23–27]. Upon implantation, the pre-vascularized constructs exhibited blood perfusion within 3 days of implantation. Moreover, the constructs revealed a hypoimmunogenic nature without active ongoing inflammation *in vivo* over 28 days. Overall, the patency, perfusability, and immunogenicity of pre-vascularized tissue constructs strongly confirmed its potential as a building block to fabricate anatomical scale 3-D pre-vascularized tissues for diverse tissue-engineering applications.

2. Results

2.1. Integrity of engineered microvascular networks upon macrophage co-culture

Anisotropic and isotropic hDF-ECM sheets were used as a scaffold to support and guide micro-vessel formation in aligned or random orientations, respectively (Fig. S1). These hDF-ECM can be developed in a desired size and shape. hDF-ECM can be stored at −80 °C and can readily be used to engineer pre-vascularized constructs. hMSCs and HUVECs were co-cultured on hDF-ECM scaffolds under optimal oxygen concentrations, to develop self-assembled microvascular networks as illustrated in Fig. 1. To mimic innate immune responses towards the pre-vascularized constructs *in vitro*, PMA-stimulated THP-1 macrophages were seeded onto pre-vascularized constructs (hMSC/EC/MP) or hMSC-only constructs (hMSC/MP) (Fig. 1). Z-stacking in confocal staining was performed to individually measure the thickness of hDF-ECM as well as the pre-vascularized layer (hMSC/EC-only layer). Pre-vascularized constructs (hMSC/EC/hDF-ECM) were stained with F-actin (red), CD31 (green) and DAPI to image the hMSC/EC-only layer, which was measured as 13.64 ± 1.70 μm thick (Figs. S1D and F). Similarly, the thickness of hDF-ECM, prior to any cell seeding was measured by staining the hDF-ECM scaffolds with two of the most abundant ECM markers, collagen-I and fibronectin, which combinedly indicated the average thickness of hDF-ECM was 50.06 ± 14.02 μm (Figs. S1E and F). These results indicated that the thickness of the entire pre-vascularized construct (hMSC/EC/hDF-ECM) was 63.70 ± 15.72 μm (Fig. S1F). Prior to the subcutaneous implantation, these large constructs were folded twice before implantation to create a multi-layered 3-D construct with the final area of ~2.2 cm2 and thickness 254.80 ± 62.87 μm.

Prior to the co-culture with pre-vascularized constructs, THP-1 monocytes were differentiated into macrophages via PMA (50 ng/mL) stimulation. Upon PMA stimulation, THP-1 cells showed increased cell adhesion, cell spreading and expression of macrophage specific markers (CD68, CD11b, CD14, EGR2) as observed via immunofluorescence (IF) staining (Fig. S2A). In addition, the mRNA expression of macrophage-specific markers (CD14, CD68, CD80) were also significantly increased ($p < 0.001$) (Fig. S2B), indicating successful differentiation of monocytes into macrophages. The representative density and morphology of THP-1 derived macrophages co-cultured onto aligned and random hMSC-only constructs (hMSC/MP) can be observed in Fig. S2C. Macrophages co-cultured onto the hMSC construct for 3 and 7 days can distinctively be observed via IF staining targeting the CD68 marker (Fig. S2C).

Microvascular networks co-cultured with macrophages were characterized via measurement of (1) vessel length, (2) vessel diameter, (3) intercapillary distance and (4) percentage area covered by micro-vessels at days 3 and 7 post macrophage seeding (Fig. 2). Aligned and randomly organized pre-vascularized constructs without macrophages (hMSC/EC) were used as a control to evaluate aforementioned characteristics of the microvascular network (Fig. 2A). At day 3, microvascular networks co-cultured without (hMSC/EC) or with macrophages (hMSC/EC/MP) showed overall similar characteristics in both aligned and random groups. The hMSC/EC (386 ± 296 μm) group showed increased vessel length compared to hMSC/EC/MP (305 ± 255 μm) on aligned constructs, but no significant difference was observed on random constructs (Fig. 2B). Aligned constructs showed significantly increased vessel length compared with random constructs in the presence (hMSC/EC/MP) ($p < 0.01$) or absence of macrophages (hMSC/EC) ($p < 0.0001$) due to the anisotropic orientation of micro-vessels (Fig. 2B). However, post 7 days of macrophage seeding, the vessel length in hMSC/EC/MP group (183 ± 116 μm in align group and 141 ± 60 μm in random group) was significantly reduced compared with the control (hMSC/EC (without macrophages) in both aligned (250 ± 206 μm) ($p < 0.05$) and random (244 ± 233 μm) ($p < 0.0001$) groups (Fig. 2B). No significant difference in the percentage area covered by micro-vessels was observed between aligned and random constructs co-cultured with macrophages (hMSC/EC/MP) at day 3. However, at day 7, the hMSC/EC/MP group showed a significant decrease in the percentage area in both aligned (4.23 ± 2.45 μm^2) ($p < 0.0001$) and randomly organized (4.07 ± 0.74 μm^2) constructs compared with the hMSC/EC group ($p < 0.05$) (Fig. 2C). Similarly, at day 7, the intercapillary distance was significantly increased in hMSC/EC/MP group in both aligned (111.31 ± 73.86 μm) ($p < 0.0001$) and random (85.60 ± 45.32 μm) ($p < 0.01$) constructs compared with the hMSC/EC group due to the reduction in microvascular network density (Fig. 2D). The self-assembled micro-vessels showed diameters

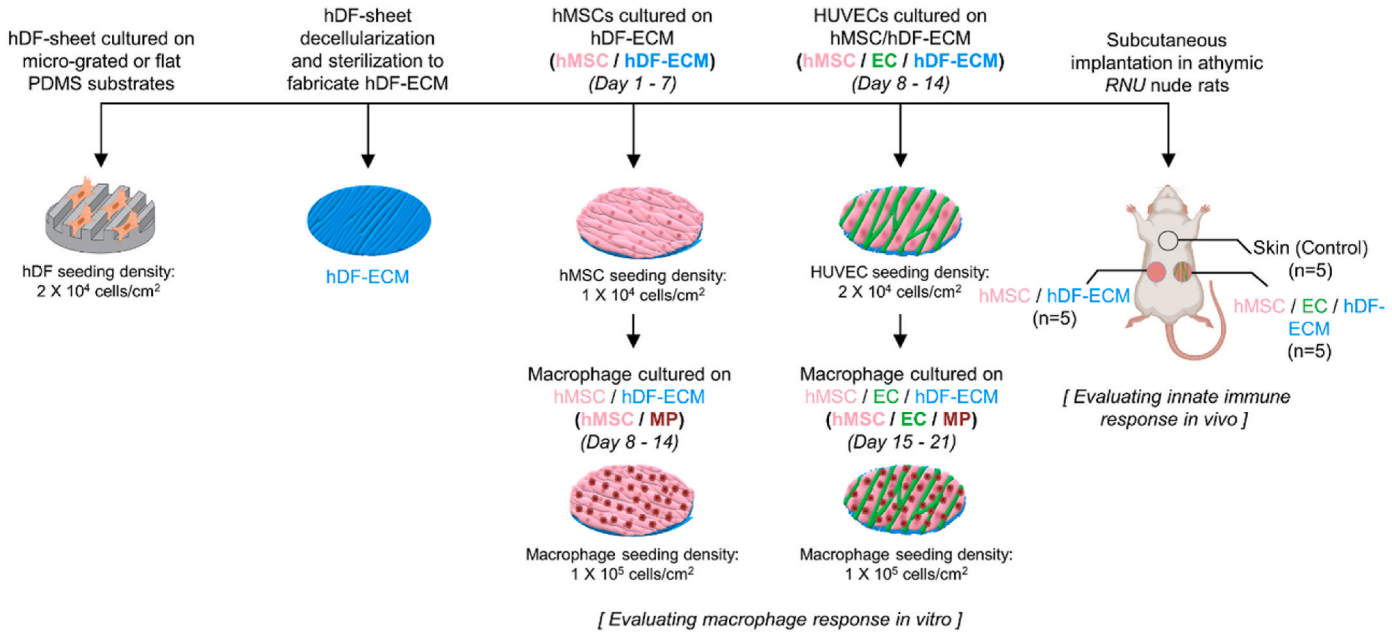

Fig. 1. Schematic illustration of pre-vascularized construct development. Immunological evaluation was performed *in vitro* and *in vivo* via macrophage co-culture and subcutaneous implantation in *RNU* nude rats, respectively.

ranging from 4 to 12 μm, which is at a similar scale as native capillaries. At day 3, no significant difference in micro-vessel diameter was observed between aligned or randomly organized micro-vessels without (aligned: 7.22 ± 3.48 μm, random: 8.13 ± 3.33 μm) or with macrophages (aligned: 8.28 ± 2.34 μm, random: 9.29 ± 4.77 μm) (Fig. 2E). However, at day 7, the hMSC/EC/MP groups (aligned: 10.13 ± 3.45 μm, random: 9.34 ± 2.39 μm) showed significantly increased vessel diameter compared with hMSC/EC (aligned: 8.09 ± 1.96 μm, random: 7.08 ± 3.22 μm) groups in both aligned ($p < 0.01$) and randomly ($p < 0.0001$) organized constructs (Fig. 2E).

Z-stacked confocal images revealed that both aligned and randomly organized micro-vessels have a tubular structure with an open lumen (Fig. 3). Pre-vascularized constructs without (hMSC/EC) or with macrophage (hMSC/EC/MP) co-culture showed similar tubular structures as observed from the CD31 signal (green). A clear lumen was observed in the cross-sectional view from z-stacked images (white arrows) (Fig. 3A). Although no difference in micro-vessel structure was observed between hMSC/EC and hMSC/EC/MP groups at day 3, a reduction in micro-vessel length and integrity was observed at day 7 in constructs co-cultured with macrophages (hMSC/EC/MP) as compared with the hMSC/EC group (Fig. 3B).

2.2. Label-free assessment of macrophage response towards pre-vascularized constructs

Metabolic status of macrophages co-cultured with hMSCs only (hMSC/MP) or pre-vascularized constructs (hMSC/EC/MP) was evaluated via FLIM. FLIM based detection of NAD(P)H and FAD has been applied as a label-free approach to evaluate the metabolic perturbations of the cells and tissues [28–31]. FLIM measures the time a fluorophore remains in the excited state before returning to the ground state by emitting a photon [32]. The lifetime of NAD(P)H and FAD within the cells can be fitted to a two-component exponential decay curve, which resolves the lifetime and corresponding fractions of different conformations, protein-bound and free. Since the bound NAD(P)H lifetime is decided by the binding protein and affiliated with different metabolic pathways, the variations in the NAD(P)H bound-fraction and lifetime have been used to indicate shifts in the metabolic pathways [33–35]. Here, autofluorescence lifetime imaging reveals differences in fluorescence lifetimes of free and bound fractions of NAD(P)H and FAD of macrophages, co-cultured on aligned and random hMSCs/MP and hMSC/EC/MP constructs (Fig. 4, S3). Due to the spatial separation of macrophages from the hMSCs and ECs, the FLIM data is exclusively from macrophages. In representative autofluorescence lifetime images of NAD(P)H and FAD of macrophages, the nuclei are darker than the cytoplasm because both NAD(P)H and FAD mainly exist in the mitochondria and cytosol (Fig. 4A). The FLIM data revealed metabolic differences within the macrophages between the 3 and 7 day time points. On day 7, the macrophages have a lower fraction of free NAD(P)H (α_1) than on day 3 (Fig. 4B), consistently for both hMSC/MP and hMSC/EC/MP (aligned and random) constructs. The macrophages on aligned hMSC/MP constructs have a shorter lifetime of free NAD(P)H (τ_1) on day 7 compared with day 3 (Fig. 4C). Conversely, the lifetimes of free and bound NAD(P)H (τ_1, τ_2) in macrophages from aligned or random hMSC/EC/MP constructs were longer on day 7 compared to day 3 (Fig. 4C and D). Consequently, macrophages from hMSC/MP (random) and hMSC/EC/MP (aligned/random) exhibit a significantly longer mean fluorescence lifetime (τ_m) on day 7 compared to day 3 (Fig. 4E).

Additionally, FLIM revealed differences in macrophage autofluorescence lifetimes between macrophages seeded on pre-vascularized constructs and immunomodulatory hMSC-only constructs. A lower fraction of free NAD(P)H (α_1) was observed for macrophages on random scaffolds with hMSC/EC/MP than random scaffolds with hMSC/MP on both day 3 and day 7 (Fig. 4B). Additionally, the lifetimes of free and bound NAD(P)H (τ_1, τ_2) are longer in macrophages on hMSC/EC/MP (random) compared to macrophages on hMSC/MP (random), which results in a longer mean NAD(P)H lifetime (τ_m) on day 3 and day 7 (Fig. 4C, D, E). Similar differences in NAD(P)H lifetime metrics, a lower fraction of free NAD(P)H (α_1) and longer lifetimes of free and bound NAD(P)H (τ_1, τ_2) were observed on day 7 for macrophages on hMSC/MP (aligned) compared with macrophages on hMSC/EC/MP (aligned) (Fig. 4C, D, E). The macrophages on all scaffolds on day 7 have an increased fraction of bound FAD (α_1) and a shorter lifetime of both free and bound FAD (τ_1, τ_2) than macrophages on day 3 (Fig. S3 A, B, C). These FAD lifetime variations lead to a shorter FAD mean lifetime (τ_m) of macrophages on day 7 compared to the mean FAD lifetime on day 3 (Fig. 4F).

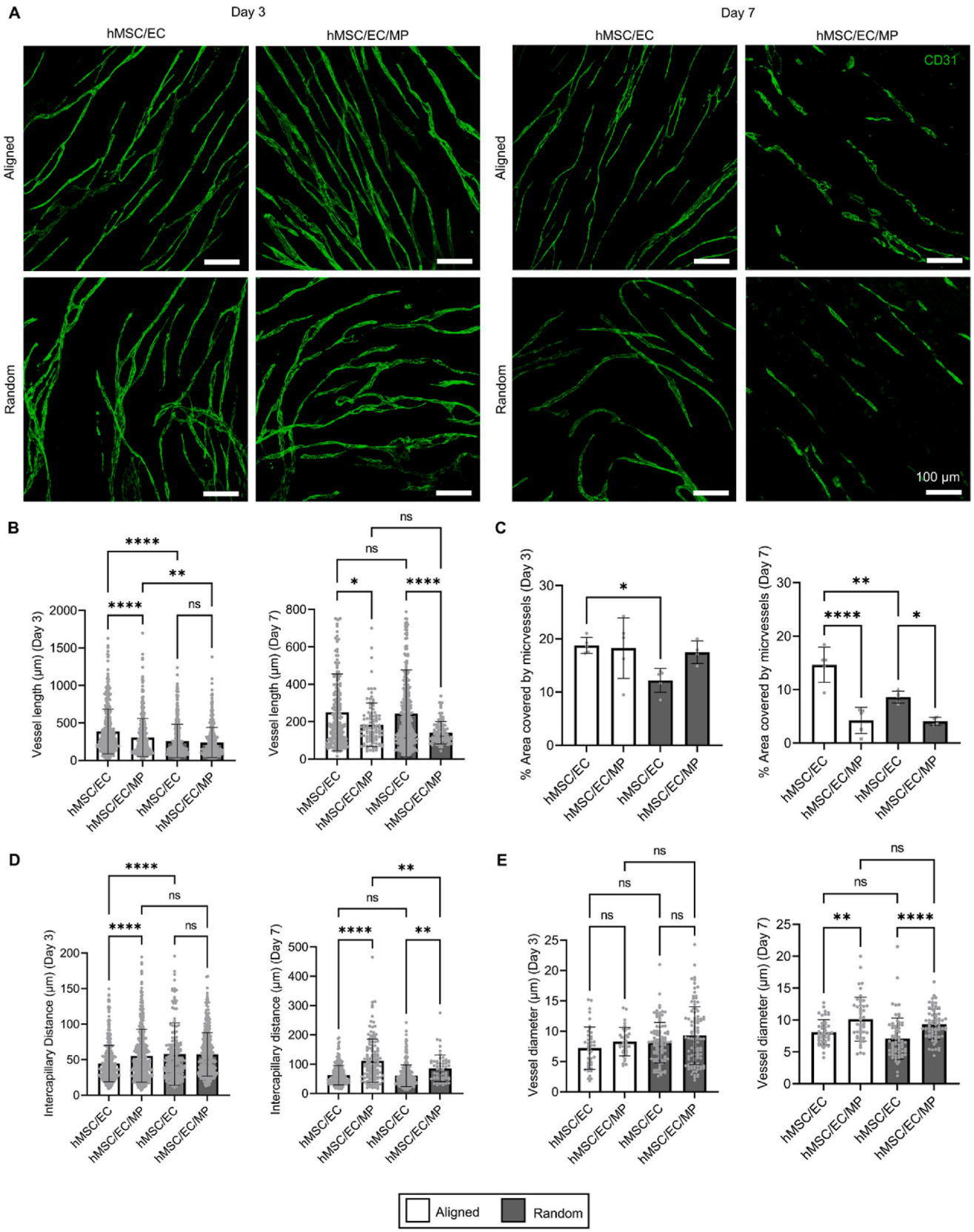

Fig. 2. Characterization of microvascular networks *in vitro*. (A) EC-specific CD31 staining (green) revealed the organization of self-assembled microvascular networks on aligned or randomly organized hDF-ECM constructs. Microvascular networks were observed post 3 and 7 days of macrophage co-culture (hMSC/EC/MP) and were compared with pre-vascularized constructs without macrophage co-culture (hMSC/EC) as a control. Scale bar: 100 μm. Microvascular networks characterized via measurement of vessel length **(B)**, area covered by micro-vessels **(C)**, intercapillary distance **(D)**, and vessel diameter **(E)**. Overall, aligned vessels showed overall increased length and vascular density compared with randomly organized vessels irrespective of macrophage co-culture. Results displayed as mean ± standard deviation and were considered statistically significant for $*p < 0.05$, $**p < 0.01$, $***p < 0.001$, $****p < 0.0001$.

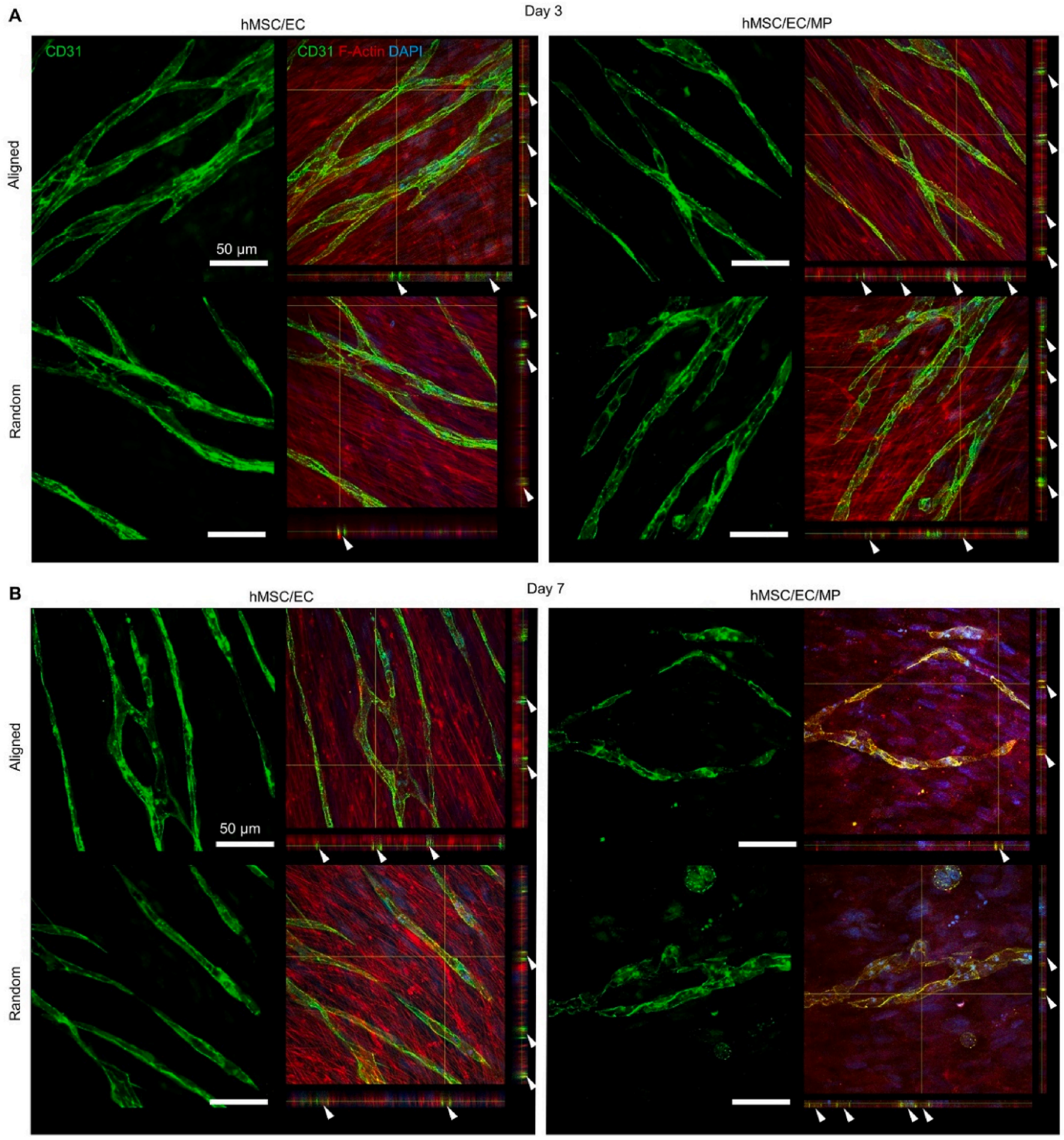

Fig. 3. Evaluation of tubular structure and lumen formation. A cross sectional view from z-stacked images of micro-vessels observed at days 3 **(A)** and 7 **(B)**, with or without macrophage co-culture revealed tubular structures (CD31, green) and a clear open lumen (white arrows). Microvascular constructs were stained with EC-specific protein CD31 (green), F-actin (red) and DAPI (blue) (Scale bar 50 μm). A majority of the micro-vessels focused in the field of view showed a clear open lumen structure irrespective of macrophage presence, indicating their excellent patency.

2.3. Metabolic status of pre-vascularized constructs during macrophage co-culture

The overall inflammatory status of the entire pre-vascularized construct co-cultured with macrophages was evaluated via western blotting and human cytokine array. The immunogenicity of pre-vascularized constructs (hMSC/EC/MP) was compared with immunomodulatory hMSC-only constructs (hMSC/MP) lacking allogenic ECs, as a control. It is known that the inflammatory status of macrophages is mainly governed by glycolysis. To determine the immunogenic status of these constructs with macrophage co-culture, glycolysis associated (pro-inflammatory) markers (glucose transporter-1 (GLUT-1), hexokinase-2 (HK2)) and regenerative macrophage specific phenotypic markers (CD163, Arginase-1 (ARG1)) were evaluated

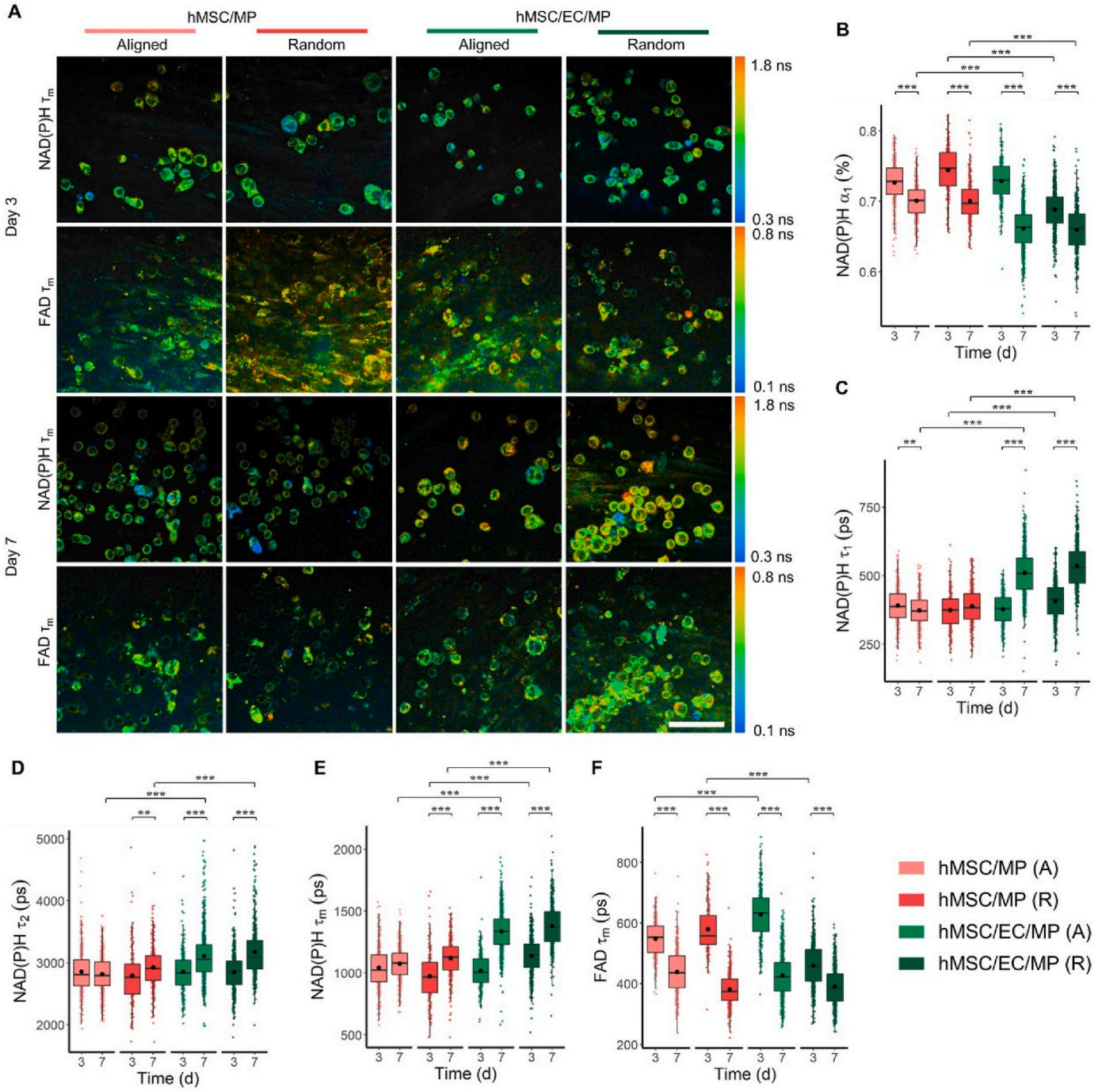

Fig. 4. FLIM-based label-free assessment of macrophage metabolism (A) Representative NAD(P)H and FAD τ_m ($\tau_m = \alpha_1{}^*\tau_1 + \alpha_2{}^*\tau_2$) images of macrophages on aligned (first and third columns) or random (second and fourth columns) constructs, 3 (first two rows) and 7 (bottom two rows) days after cell-seeding. Scaffolds were seeded with hMSCs and macrophages without (first two columns) and with ECs (last two columns). Scale bar = 90 μm **(B)** NAD(P)H free fraction α_1 **(C)** NAD(P)H lifetime of the free fraction τ_1 **(D)** NAD(P)H lifetime of the bound fraction τ_2 **(E)** NAD(P)H mean lifetime τ_m and **(F)** FAD mean lifetime τ_m of macrophages on scaffolds with aligned and random fibers with and without ECs on days 3 and 7 post-cell seeding. Results displayed as mean ± standard deviation and were considered statistically significant for $^*p < 0.05$, $^{**}p < 0.01$, $^{***}p < 0.001$, $^{****}p < 0.0001$ (A: aligned, R: random).

(Fig. 5). It was observed that the hMSC/EC/MP showed increased expression of HK2 from day 3 to day 7 compared with hMSC/MP in both aligned and random groups (Fig. 5B). Similarly, aligned and random hMSC/EC/MP constructs showed increased expression of GLUT-1 receptor from day 3–7 compared to hMSC/MP constructs (Fig. 5C). Consistently, reduced expression of M2 macrophage-associated marker CD163 was observed from day 3 to day 7 in hMSC/EC/MP groups (aligned and random) compared with hMSC/MP group (Fig. 5D). No change in early growth response 2 (EGR2) expression was observed at day 3 between hMSC/EC/MP and hMSC/MP group. However, a reduced expression of EGR2 was observed in hMSC/EC/MP group compared with hMSC/MP group in both aligned and random constructs (Fig. 5E). Although ARG1 expression was higher in hMSC/EC/MP group compared with hMSC/MP group at day 3, it reduced to similar levels in both groups at day 7 (Fig. 5F). Both hMSC/MP and hMSC/EC/MP group showed similar expression of EGR2 at day 3 and day 7 (Fig. 5F). One of the well-studied immunomodulatory mechanisms by which hMSCs promote a macrophage shift from an inflammatory to regenerative

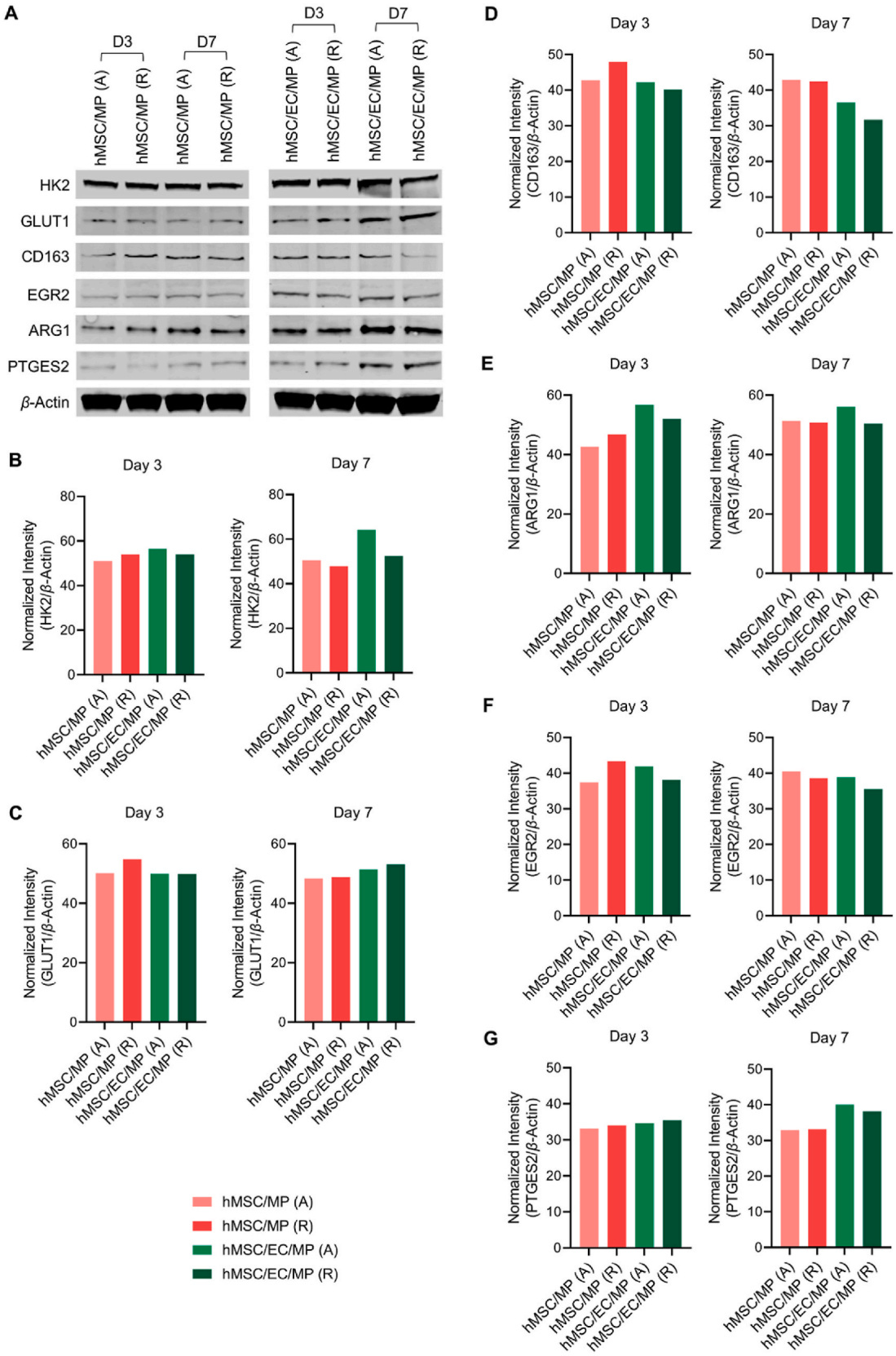

Fig. 5. Phenotypic expression of macrophage specific pro-inflammatory and regenerative markers. (A) Expression of pro-inflammatory and regenerative proteins in hMSC/MP and hMSC/EC/MP constructs on day 3 and day 7. **(B–G)** Normalized pixel intensity of proinflammatory (HK2, GLUT1), anti-inflammatory/regenerative (CD163, ARG1, EGR2) and immunomodulation markers (PTGES2) against β-actin (A: Aligned, R: Random). Overall, prevscularized constructs co-cultured with macrophage (hMSC/EC/MP) at day 7 showed increased expression of pro-inflammatory and reduced expression of anti-inflammatory protein markers compared to the other experimental groups.

phenotype is by secretion of prostaglandin E synthase 2 (PTGES2) [36]. Both aligned and random hMSC/EC/MP groups showed increased expression of PTGES2 from day 3 to day 7 compared with the hMSC/MP group, indicating an increased activation of this immunomodulatory mechanism over time (Fig. 5G).

Results obtained from micro-vessel characterization, FLIM and western blotting indicated that the pre-vascularized constructs co-cultured with macrophages (hMSC/EC/MP) for 7 days showed decreased density of microvascular networks and increased activation of pro-inflammatory markers. To further delineate the overall immunogenic status of hMSC/EC/MP constructs at day 7, the conditioned media and cell lysates were analyzed via a human cytokine array and compared with hMSC/MP constructs (Fig. 6). Fluorescent intensities of 49 cytokines and surface markers were detected and classified under 3

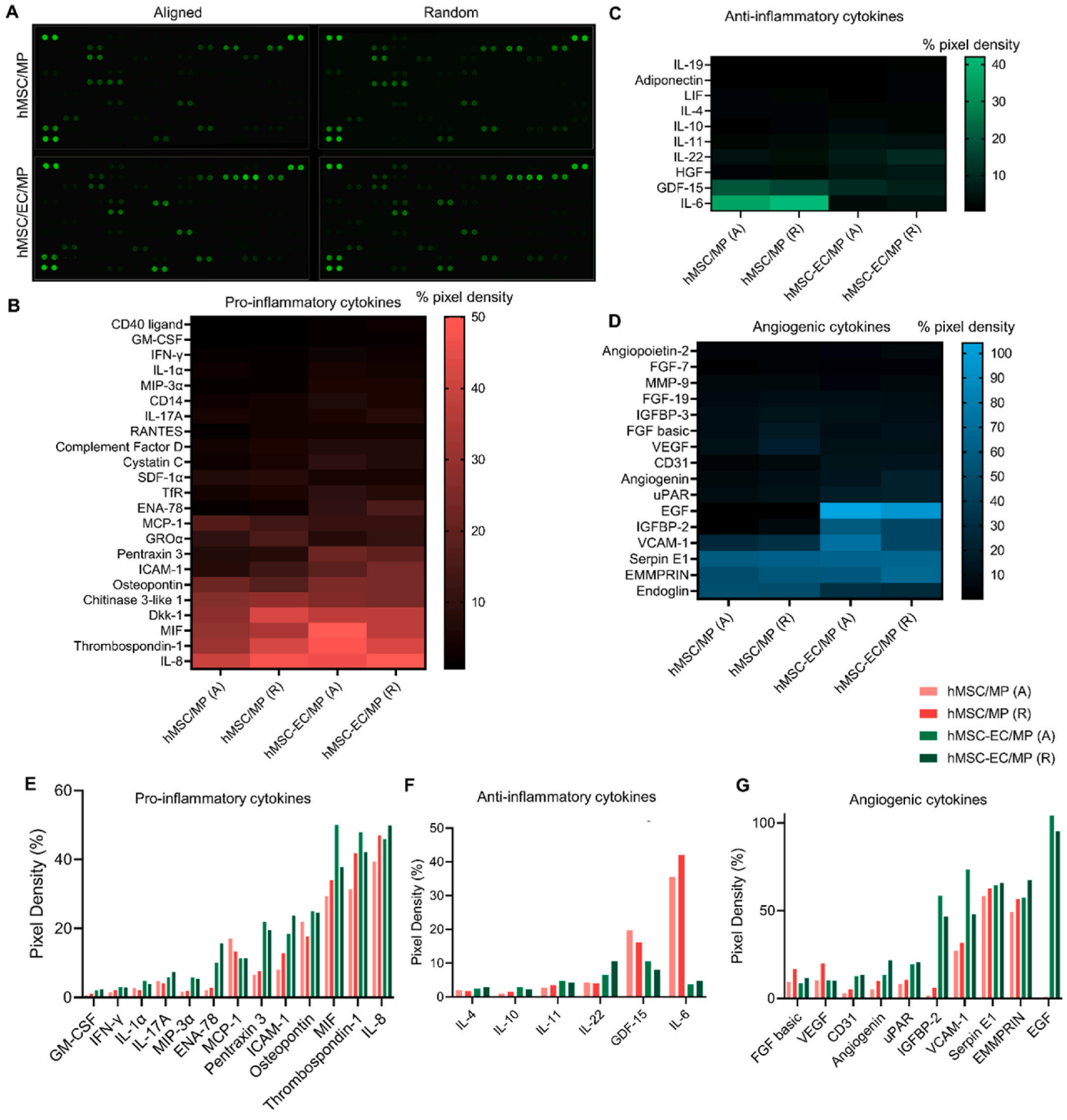

Fig. 6. Human cytokine array. (A-D) Proinflammatory, anti-inflammatory and angiogenic cytokines detected from macrophage co-cultured pre-vascularized (hMSC/EC/MP) and hMSC constructs (hMSC/MP) post 7 days of macrophage seeding. **(E–G)** quantification of percentage pixel density for pro-inflammatory **(E)**, anti-inflammatory **(F)**, and angiogenic cytokines **(G),** detected from day 7 hMSC/MP and hMSC/EC/MP constructs (A: Aligned, R: Random). Overall, pre-vascularized constructs showed slightly higher levels of pro-inflammatory, and angiogenic cytokine/surface receptor expression compared to the immunomodulatory hMSC/MP group.

categories including pro-inflammatory cytokines (Fig. 6B), anti-inflammatory cytokines (Fig. 6C) and angiogenic cytokines (Fig. 6D). It was observed that hMSC/EC/MP constructs showed similar expression of proinflammatory cytokines interferon gamma (IFN-γ), interleukin (IL)-1α, IL-8, IL 17, granulocyte-macrophage colony-stimulating factor (GM-CSF), compared with the hMSC/MP group (Fig. 6E). However, hMSC/EC/MP showed increased expression of epithelial-derived neutrophil-activating protein 78 (ENA 78), intercellular adhesion molecule (ICAM)-I, macrophage migration inhibitory factor (MIF) compared to the hMSC/MP group (Fig. 6E). IL-6 was significantly reduced in hMSC/EC/MP compared to hMSC/MP (Fig. 6E). It has been reported that bone marrow derived hMSCs promote immune-suppression via secretion of IL-6 [37]. Correspondingly, hMSC co-cultured with macrophage (hMSC/MP) showed increased levels of IL-6 (Fig. 6E). Moreover, it was observed that the aligned constructs showed reduced levels of IL-8 and ICAM-I compared to random constructs in both hMSC/MP and hMSC/EC/MP groups (Fig. 6E), Overall, hMSC/EC/MP constructs showed a slightly higher expression profile of pro-inflammatory cytokines compared to the hMSC/MP group (Fig. 6B), supporting the phenomena observed in FLIM and western blotting. Aligned and random hMSC/EC/MP constructs had similar levels of anti-inflammatory cytokine IL-4, IL-10, IL-11, but higher levels of IL-22, macrophage inflammatory protein 3 alpha (MIP-3a), pentraxin-3 compared to hMSC/MP constructs (Fig. 6F). IL-10 and IL-22 have proven roles in preventing inflammatory responses and in promoting tissue regeneration [38]. hMSC/EC/MP constructs showed slightly increased expression of IL-10 and IL-22 compared to hMSC/MP constructs (Fig. 6F). It was observed that aligned hMSC/EC/MP constructs showed increased levels of pentraxin-3 and growth/differentiation factor (GDF)-15 compared to random constructs, while IL-22 levels were higher in random constructs compared to the aligned group (Fig. 6F). hMSC/EC/MP constructs showed higher secretion of angiogenic cytokines urokinase-type plasminogen activator receptor (uPAR), insulin-like growth factor-binding protein (IGFBP)-2, Serpin E1 and extracellular matrix metalloproteinase inducer (EMMPRIN) compared to hMSC/MP constructs (Fig. 6G). In pre-vascularized group (hMSC/EC/MP), increased levels of IGFBP-2 and vascular cell adhesion protein (VCAM)-1 were observed in aligned constructs, while increased levels of angiogenin, serpin E1 and EMMPRIN were observed in random constructs (Fig. 6G).

2.4. Assessment of anastomotic capability and immunogenicity of pre-vascularized constructs in vivo

hMSC-only or pre-vascularized constructs (hMSC/EC) developed on hDF-ECM were subcutaneously implanted in *RNU* nude rats and harvested at days 3, 7, 14 and 28 post implantation. Histological analysis of the implants and the recruitment of host cells surrounding the implants in the subcutaneous space were determined via H&E staining. (Fig. S4). A continues reduction of cellular recruitment surrounding the implants in the subcutaneous space over 28 days (as observed by purple nuclei signal) indicated a possible resolution of inflammation and a lack of continuous active inflammation (Fig. S4). The implanted cells remain viable until day 28 at the implant site as observed via hNA staining that co-localized with DAPI signal (Fig. 7A). The hNA signal was only present within the boundary of implant (indicated as white dotted line) and was absent elsewhere, clearly indicating the implanted allogenic cells survived for 28 days (Fig. 7A, bottom row). To determine the anastomotic capability and perfusability of engineered micro-vessels, biotinylated UEA-I, which specifically binds with functional human ECs was injected systemically in the left ventricle of rats prior to euthanization. Besides UEA-1 (green), vessels were co-stained with polyclonal antibody targeting CD31 (red) which can bind with rat/human ECs (Fig. 7B). The presence of UEA-1 signal in the subcutaneous implantation area clearly proves that the engineered human micro-vessels remained patent and were anastomosed with the host vasculature within one week of implantation (Fig. 7B). Magnified images of UEA-1 positive engineered micro-vessels with lumen surrounding a single EC were observed (Fig. S5 A), which clearly indicated anastomosis with host vasculature and a successful blood perfusion. Higher magnification images revealed UEA-1 positive micro-vessel lumens surrounded by a single EC containing a single nuclei (Fig. S5 B) from skin samples harvested after 3 days of implantation, which provided evidence that the engineered micro-vessels became perfused within 3 days of implantation. In addition, a possible remodeling of engineered micro-vessels was also observed with an increasing period of time post implantation. The significant increase in the diameter of UEA-1 positive micro-vessels was observed from day 3 (14.42 ± 8.30 μm) to day 7 (22.88 ± 9.47 μm) ($p < 0.001$), day 14 (21.71 ± 8.95 μm) ($p < 0.001$) and day 28 (23.96 ± 11.84 μm) ($p < 0.001$). The diameter of UEA-1 positive lumens (14.42 ± 8.30 μm) detected at day 3 was similar to the micro-vessel diameters measured *in vitro* (Fig. 2E). No significant change in UEA-1 positive vessel diameter was observed from day 7 to day 28 (Fig. 2E).

The immunogenicity of implanted constructs was evaluated by determining the recruitment of CD68 positive macrophage at the implant site. The subcutaneous tissues containing hDF-ECM scaffolds with only hMSCs (hMSC/hDF-ECM) (Fig. 8A) or micro-vessels (hMSC/EC/hDF-ECM) (Fig. 8B) were harvested to evaluate recruitment of macrophages. Macrophage infiltration from skin samples harvested from non-implanted regions far away from the hMSC/hDF-ECM and hMSC/EC/hDF-ECM implant site were used as a control (Fig. 8C). Macrophage recruitment surrounding the implant site was evaluated over the study period to understand the timeline for ongoing immune responses. Both hMSC/hDF-ECM and hMSC/EC/hDF-ECM showed a similar number of recruited macrophages over the 28 day period (Fig. S6). Although hMSC/EC/hDF-ECM group had slightly increased recruitment of macrophages compared to hMSC/hDF-ECM group at days 3, 14 and 28, the difference was not significant (Fig. S6). Both implants had a significantly increased number of recruited macrophages compared to the control skin (Fig. S6) ($p < 0.0001$). The significant increase in the number of recruited macrophages was observed from day 3 to day 7 in both constructs (Fig. 8D and E). Macrophage counts reached a maximum value at day 7 and then gradually reduced. A significant reduction in macrophage number was observed at day 14 compared to day 7 in both hMSC/hDF-ECM and hMSC/EC/hDF-ECM implants (Fig. 8D and E). The number of recruited macrophages was significantly reduced at day 28 compared with the other three time points for both implants (Fig. 8D and E), indicating a resolution of inflammation over time. No significant difference was observed for recruited macrophage number in the subcutaneous space of the control skin samples over the 28-day observation period (Fig. 8F).

3. Discussion

One of the critical bottlenecks in engineered anatomical-scale tissues is a lack of built-in functional vasculature, which is essential to ensure exchange of gases, nutrients, and cell secreted toxins post implantation. Ideally, anatomical-scale built-in micro-vessels, that form a functional anastomosis with host vasculature within a few days, should be contained within the engineered tissue-construct to ensure graft survival. In addition, the engineered microvasculature should withstand physiological pressure without any leakage or elicit a negative immune response [39]. Microvascular networks in native tissues are organized in a hierarchical order to ensure optimal molecular exchange and function [3]. Most recent advances in the field of microfluidics have enabled self-assembly of microvascular networks within a hydrogel and tested their perfusability and potential of disease modelling and drug screening [6–8]. Several leading groups have investigated a co-culture-based approach to engineer micro-vascular networks via co-culturing endothelial cells (i.e., HUVECs, human embryonic stem cell-derived ECs, endothelial progenitor cell–derived ECs, or endothelial colony forming cells) with stomal or perivascular cells (i.e., MSCs, fibroblasts) in a

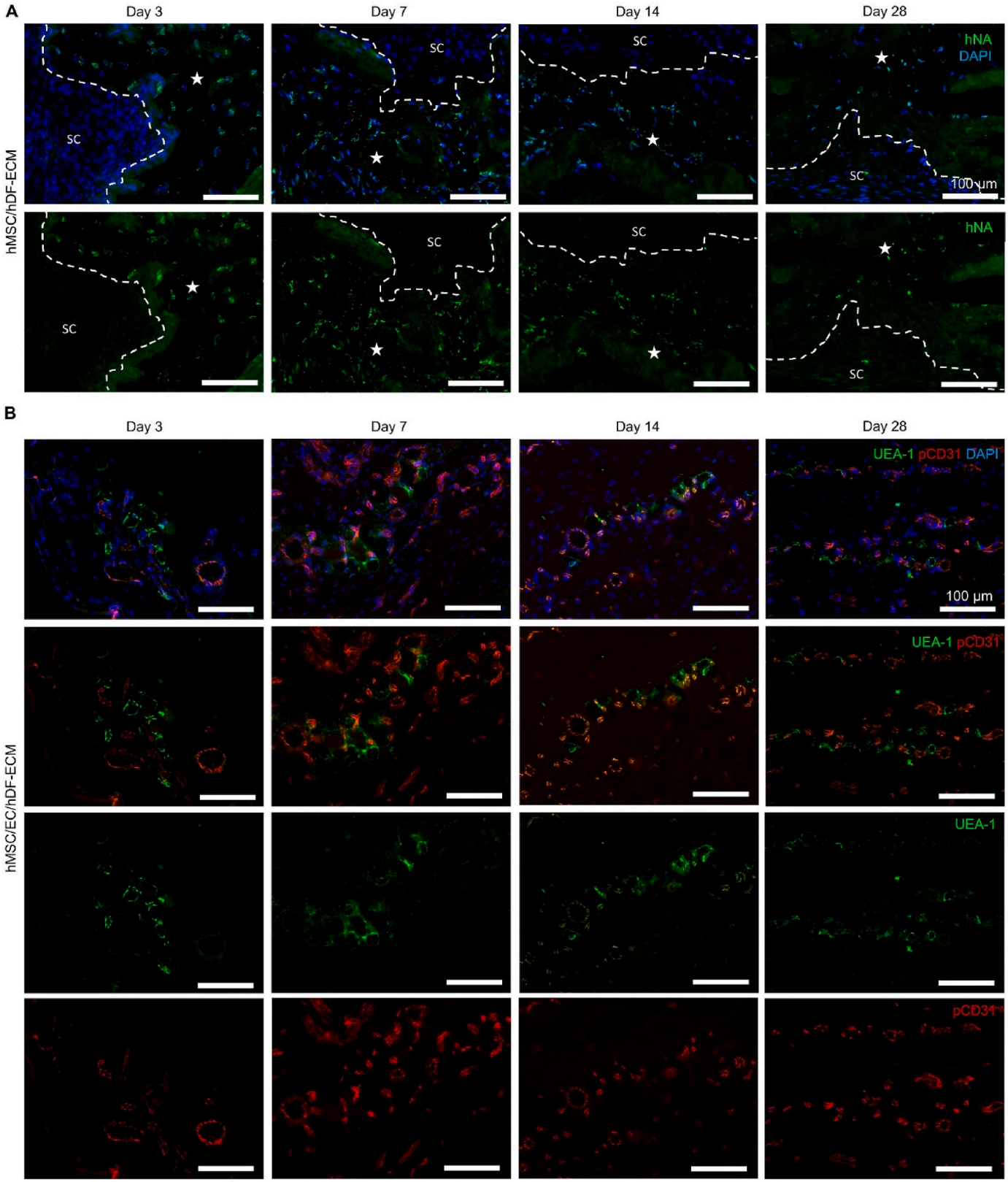

Fig. 7. Evaluation of engineered constructs post-subcutaneous implantation in RNU nude rats. (A) Positive hNA signal (green) indicated presence of human cells from day 3 to day 28 at the implant site (white star) but absent in the subcutaneous space (SC). (B) Microvascular lumens stained with UEA-1 lectin (green) were observed in the subcutaneous space at days 3, 7,14 and 28, indicating a successful anastomosis. Micro-vessels were co-stained polyclonal CD31 (red), which targets ECs with human/rat origin. A positive hNA signals indicated that the constructs survived for 28 days in the subcutaneous space. UEA-1 positive lumen structures found in the subcutaneous space confirmed that human capillaries maintained open lumen structure and formed a functional anastomosis with host vessels within 3 days of implantation (Scale bar 100 μm).

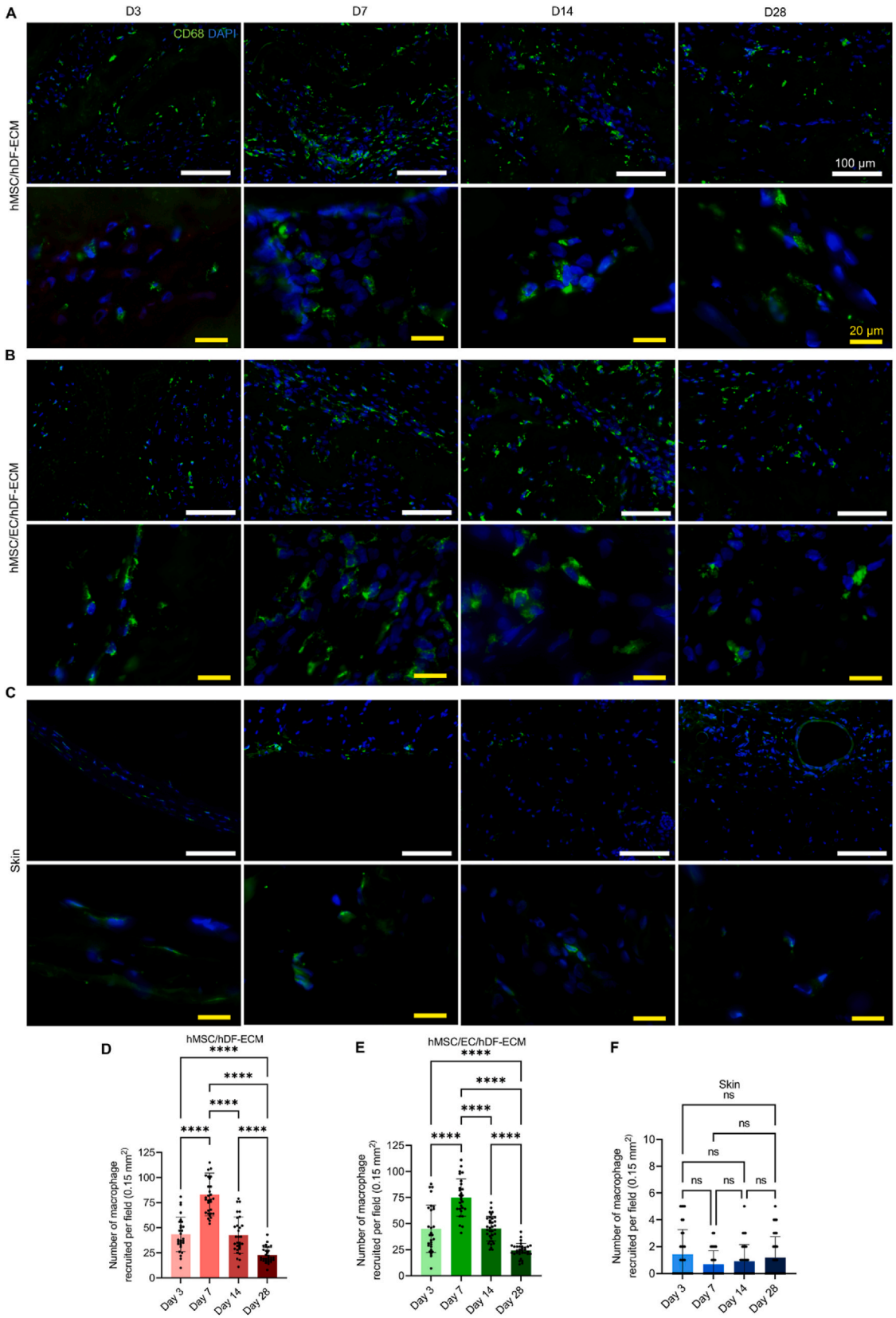

Fig. 8. Evaluation of macrophage recruitment *in vivo*. Positive CD68 signal (green) indicated presence of recruited macrophage from day 3 to day 28 surrounding (A) hMSC/hDF-ECM implant, (B) hMSC/EC/hDF-ECM implant and (C) skin (control). (Scale bars white: 100 μm, yellow: 20 μm) Quantification of number of recruited macrophage surrounding implants hMSCs/hDF-ECM (D) and hMSC/EC/hDF-ECM (E) and their comparison with control skin (without any implant) (F) at days 3, 7, 14 and 28 post-implantations. Overall, increased macrophage recruitment was observed during the first week of implantation, which eventually reduced over time and indicated a lack of ongoing active inflammation. Results displayed as mean ± standard deviation and were considered statistically significant for $*p < 0.05$, $**p < 0.01$, $***p < 0.001$, $****p < 0.0001$.

scaffold-free or hydrogel based (collagen and fibrin) constructs and proved their perfusion *in vivo* [40–43]. In the current study, we aimed to engineer readily transplantable pre-vascularized beds on ECM-sheets with dense micro-vascular networks, which can be employed to build diverse, anatomical scale-large tissues. Compared to the traditionally used ECM mimicking hydrogels, our hDF-ECM provides a superior compositional complexity as it is a cell-secreted ECM containing myriads of structural, non-structural and matricellular proteins, polysaccharides, and other small molecules. Moreover, the hDF-ECM developed via soft-lithography approach provides an architectural tunability to guide the deposition of hDF-secreted ECM in a tissue-specific direction by altering size and/or shape of micro-structures, to ultimately control the directionality of micro-vessel growth. To further validate its potential to engineer large tissue-constructs, the current study evaluated the patency, anastomotic capability, perfusability and the innate immune response toward these pre-vascularized hDF-ECM sheets *in vitro* and *in vivo*.

The aligned and randomly organized micro-vascular networks developed on the hDF-ECM scaffold exhibited a diameter similar to native capillary beds (Fig. 2) [44]. Consistent with our previous observation, aligned nano-fibrous hDF-ECM architecture showed increased micro-vessel length and density compared with micro-vessels developed on randomly organized ECM irrespective of macrophage-co-culture (Fig. 2). Importantly, self-assembled micro-vessels with diameters as small as < 20 μm showed a clear open lumen, confirming their tubular structures (Fig. 3). To evaluate immunogenicity of engineered constructs *in vitro*, macrophages were co-cultured with pre-vascularized constructs and compared with immunomodulatory hMSC-only constructs. The pre-vascularized constructs maintained micro-vascular density for 3 days but exhibited significant degradation in vessel density after 7 days, indicating a macrophage-mediated destruction of micro-vessels (Fig. 2A). It is known that pro-inflammatory macrophage activation is dependent on anaerobic glycolysis, while anti-inflammatory macrophages rely on aerobic respiration, such as oxidative phosphorylation (OXPHOS), for their energy demands [45]. These metabolic perturbations in macrophages within the pre-vascularized or immunomodulatory hMSC-only constructs were revealed by FLIM-based imaging of NAD(P)H and FAD, important co-enzymes of metabolic pathways including glycolysis, OXPHOS, and glutaminolysis [46–49]. FLIM can exclusively evaluate macrophages within the co-culture system due to the physical separation of macrophages from hMSCs and ECs at different depths within the constructs (Fig. 4, Fig. S2C). In line with the *in vitro* micro-vascular network characterization (Fig. 2), significantly increased bound NAD(P)H lifetime (τ_2) was measured in macrophages that were co-cultured with pre-vascularized constructs for 7 days (Fig. 4). The difference in NAD(P)H lifetime components was exaggerated from day 3 to day 7 in pre-vascularized construct compared with immunomodulatory hMSC only constructs, possibly due to the activation of macrophages by the non-immunomodulatory HUVECs. Consistently, in the presence of macrophages, pre-vascularized constructs post 7 days exhibited increased expression of glycolysis associated pro-inflammatory proteins (GLUT-1 and HK2) and reduced expression of anti-inflammatory proteins (CD163, EGR2, ARG1) (Fig. 5). Whereas, owing to the immunomodulatory property of hMSCs, the hMSC-only groups (aligned and random) exhibited reduced expression of HK2 and GLUT-1 (Fig. 5B and C), and increased expression of CD163 and EGR2, proteins predominantly present in anti-inflammatory phenotypes of macrophage. EGR2 is a direct target of IL-4-activated STAT6 and has a broad functionality to further induce several transcription factors driving alternative macrophage polarization [50,51]. ARG1 is a key enzyme involved in L-arginine metabolism, highly expressed in tumor-associated macrophages that have immunosuppressive and tumorigenic functions [52,53]. Compared with hMSC-only group, pre-vascularized groups had increased ARG1 expressiodsn post day 3 of macrophage-culture, which further reduced to became similar as hMSC-only groups on day 7, indicating a reduction in immunosuppressive activity of macrophages (Fig. 5E). One of the known mechanisms by which hMSCs promote immunomodulation is via secretion of PGE2, which activates production of anti-inflammatory cytokine IL-10 from macrophage to suppress the inflammatory phenotype [36,54]. The highest expressions of PGE2 (Fig. 5G) and IL-10 (Fig. 6F) were observed in day 7 pre-vascularized groups, indicating their maximum effort to suppress inflammatory response. Taken together, results obtained from IF-based characterization, FLIM, and western blotting indicated a macrophage shift towards the pro-inflammatory phenotype after 7 days of co-culture with pre-vascularized constructs, which was further verified in cytokine array analysis. Compared with the macrophage co-cultured hMSC only group, the day 7 pre-vascularized group exhibited increased secretion of GM-CSF, IFN-γ, IL-1A, IL-8, IL-17A, MIP-3A which are key regulators that stimulate macrophage activation, due to the presence of non-immunomodulatory HUVECs in the constructs [55]. Furthermore, the prevacularized group improved expression of pentraxin-3, which is associated with vascular inflammation and endothelial dysfunction [56], which could explain why micro-vessels degraded (Fig. 2A). The presence of macrophage-secreted cytokines alone can significantly promote the micro-vascular regression observed at day 7 (Fig. 2A), which could be further tested by culturing pre-vascularized constructs (without macrophage) in conditioned media obtained from macrophage co-cultured pre-vascularized constructs (hMSC/EC/MP). As expected, compared to the hMSC group, pre-vascularized constructs showed enhanced expression of angiogenic growth factors (CD31, VECAM-1, Angiogenin, IGFBP-2) [57] and proteolytic degradation of ECM (uPAR) [58], which are essential for self-assembly of micro-vasculature (Fig. 6G). Both aligned and random construct architecture promoted metabolic perturbations in macrophages, as observed via FLIM, and the immunogenicity of the entire constructs as revealed via western blot and cytokine array. However, the perturbations caused by aligned or random architectures were not as significant as those triggered by the presence or absence of non-immunomodulatory HUVECs within the constructs (Figs. 4–6, S3).

The innate immunogenicity of pre-vascularized constructs was further analyzed *in vivo* via subcutaneous implantation in athymic *Foxn1*^{rnu} nude rats. *Foxn1*^{rnu} nude rats established by the National Institutes of Health (by knocking out the *RNU* allele on chromosome 10) lack a mature thymus and are deficient in T-cells [59]. However, the innate immune system in these rats is well developed with a functional population of granulocytes, monocytes/macrophage, mast cells, natural killer cells, dendritic cells, and $CD3^+$ T-like cells without functional TCR [23]. It has been reported that *Foxn1*^{rnu} nude rats even have a stronger innate immune response compared to normal immune compatible rats [23–27]. Therefore, the *Foxn1*^{rnu} nude rodent model has strategically been used to investigate innate immune responses towards allogenic or xenogeneic implants exclusively without confounding effects from functional T cells [23]. In addition, the *RNU* rodent shows a delayed rejection of xenografts from human origin, and therefore has been commonly used to study the fate of allograft and xenograft transplants, such as for muscle regeneration [60]. In a recent study, Redd et al., also used the *Foxn1*^{rnu}-Nude rat to evaluate improved perfusion of infarcted hearts following the implantation of human microvascular xenografts [42]. In-parallel to the previous research, *Foxn1*^{rnu} nude rats were selected in the current study to investigate the role of the innate immune response on graft survival and perfusability of micro-vessels over a 28 day period. Since aligned constructs showed increased micro-vessel density compared to random constructs (Fig. 2), only aligned pre-vascularized constructs were considered for this proof-of-concept animal study.

An anticipated recruitment of host cells surrounding the implant boundary was observed during the first week. This recruitment became less evident over time, as observed by histological analysis (Fig. S4). After 4 weeks, the implant was well integrated in the subcutaneous space, without any signs of a pro-longed active inflammation (Fig. S4).

Macrophage recruitment was increased during the first week and gradually decreased over time, with minimal levels of macrophages observed at day 28 (Fig. 8). Importantly, recruited macrophages did not show significant differences in numbers between immunomodulatory hMSC-only and pre-vascularized constructs over time (Fig. S6), proving the hypo-immunogenic nature of these engineered constructs *in vivo*. In a recent study, Graney et al., investigated the influence of pro-inflammatory (M1) and pro-healing (M2a, M2c, M2f) macrophage phenotypes on the vascularization of engineered tissue [61]. Genes associated with sprouting angiogenesis were up-regulated during a short-term co-culture with M1 macrophages, while genes associated with pericyte cell differentiation were up-regulated during pro-healing macrophage co-culture. This study also delineated a crucial function of macrophages in the remodeling and anastomosis of engineered micro-vessels [61]. In addition to macrophages, Lin et al., recently revealed the significance of anti-inflammatory, pro-remodeling (N2) phenotype neutrophil recruitment and associated Notch signaling for successful vascularization [62]. The study proved that a GelMA hydrogel with pre-assembled microvessels failed to engraft upon implantation due to their inability to engage the alternative (N2) neutrophils; adoptive transfer of N2 neutrophils fully restored vascularization in the myeloid-depleted mice. Importantly, pre-assembled vessels treated with a γ-secretase inhibitor (DAPT) to block Notch signaling restored neutrophil recruitment via restored neutrophil-associated chemokines, and significantly improved micro-vessel perfusion following implantation [62].

Detecting perfusability of human-origin vessels *in vivo* via human EC-targeting UEA-1 lectin injection has been widely adopted [42,63]. UEA-1 positive lumens observed in tissues harvested post 3 days implantation indicated successful anastomosis of engineered micro-vessels within as early as 3 days of implantation. A slight increase in lumen diameter than the pre-implanted vessels was observed during the first week of implantation, suggesting a possible remodeling of the engineered micro-vasculature (Fig. S5B). However, no further increase in UEA-1 positive vessel diameter was observed after the first week, indicating the vessels were stable and not significantly dilated post perfusion (Fig. S5B). Although HUVECs were selected as a typical model EC-type in this proof-of-concept study, they can be replaced with more advanced and clinically relevant universal or hypoimmunogenic derivatives of induced pluripotent stem cell (hiPSC) derived ECs in the future, to advance one step closer towards translational applications [64,65]. In addition to maturing the self-assembled microvascular networks as pericytes, hMSCs are known to promote immunomodulation via secretion of interleukin-1 receptor antagonist (IL1RA), PGE2 and tumor necrosis factor-inducible gene 6 (TSG-6) [17,36,66] to mitigate the immune response and preserve microvascular integrity. hMSCs have been incorporated as bulk cells in the pre-vascularized construct. Their well proven multifaceted regenerative potential in several diseases [67] make the pre-vascularized construct versatile for various tissue-regenerative applications. The feasibility of creating large pre-vascularized ECM sheets that can be used as building blocks will enable tissue-engineers to fabricate anatomical scale 3-D constructs to replace damaged or diseased tissues. The faster anastomotic capabilities and perfusability of these engineered micro-vessels will greatly improve the rate of implant survival by promptly restoring the oxygen and nutrient supply, and thereby ensuring the superior functionality or regenerative capability of implanted constructs.

4. Conclusions

A completely biological and native tissue-architecture mimicking pre-vascularized hMSC-based construct was developed. The micron-scale vascular network remained patent during *in vitro* co-culture with macrophages and showed an open lumen. Results from label-free FLIM imaging and *in vitro* macrophage co-culture assays revealed the micro-vessel patency and immunogenicity of engineered constructs via detecting metabolic perturbations in co-cultured macrophages. Subcutaneously implanted constructs remained viable during 28 day course of the study. Pre-vascularized tissue constructs with self-assembled dense microvascular networks formed a functional anastomosis and showed successful perfusion within 3 days of implantation. Immunomodulatory hMSC-containing pre-vascularized constructs avoided a prolonged inflammatory responses *in vivo*. The macrophage recruitment consistently resolved one week post implantation, indicating the hypoimmunogenic nature of the constructs. Overall, the engineered microvascular networks developed on completely biological ECM matrix scaffolds closely mimic the anatomy of native capillary beds and can be used as transplantable building blocks to fabricate anatomical scale large 3-D tissues.

5. Material and methods

5.1. Anisotropic and isotropic hDF-ECM fabrication

A silicon wafer with aligned grooves (width: 5 μm, Pitch: 8 μm, height: 270 nm) was prepared with a soft lithography technique at the microfabrication shared facility (MFF) at Michigan Technological University. Polydimethylsiloxane (PDMS) molds were cased from the silicon wafer using Sylgard 184 Silicone Elastomer Kit (Dow Corning, Midland, MI) by mixing base and cross-linker at 10:1 ratio followed by heating at 65 °C for 4 h. Flat PDMS was cast from a flat plastic petri dish. Micropatterned and flat PDMS were coated with polydopamine and collagen-I prior to cell culture as described in the previous publication [68]. Briefly, PDMS were immersed in 0.01% W/V 3-hydroxytyramine hydrochloride (Dopamine-HCl) (ACROS Organics, Fisher scientific) for 24 h followed by ethylene oxide sterilization. Polydopamine coated PDMS were immersed in bovine collagen (20 μg/mL) (Sigma Aldrich, St. Louis, MO) for 2 h before cell seeding [68]. Neonatal human dermal fibroblasts (ATCC, Manassas, VA) (passage 3–5) were cultured on micropatterned and flat PDMS for 6 weeks to develop anisotropic or isotropic hDF sheets, which were then decellularized to fabricate anisotropic or isotropic hDF-ECM as described previously [14,69]. Briefly, hDF sheets were decellularized using 1 M NaCl, 0.5% Sodium dodecyl sulfate (SDS), 10 mM Tris and 5 mM ethylenediaminetetraacetate (EDTA) [14].

5.2. Pre-vascularization of hDF-ECM

Anisotropic or isotropic hDF-ECM were pre-vascularized using bone marrow derived hMSCs and human umbilical vein endothelial cells (HUVECs) as described previously [14]. Briefly, passage 3–5 hMSCs (1×10^4 cells/cm^2) (LONZA) were cultured on hDF-ECM for 7 days under physiological hypoxia (2% O_2) using a programmable hypoxia chamber (Biospherix, Inc., Parish, NY). After 7 days, passage 3–5 HUVECs (LONZA) (2×10^4 cells/cm^2) were seeded onto the hMSC-hDF-ECM and were cultured for another 7 days under physiological normoxia (21% O_2). Pre-vascularized hDF-ECM (hMSC/EC/ECM) or hMSC/ECM (without HUVEC) were implanted *in vivo* or tested *in vitro* using macrophage co-culture. For *in vivo* experiment, only aligned constructs were implanted as proof of concept. Microvascular networks were characterized via measurement of vessel length, vessel diameter, intercapillary distance and percentage area covered by micro-vessels using the EC-specific CD31 (PECAM1) marker as described previously [14].

5.3. Macrophage co-culture on tissue constructs

THP-1 monocytes (ATCC) were cultured with RPMI-1640 media (ATCC) supplemented with 10% fetal bovine serum (FBS) (R&D systems) and 1% penicillin/streptomycin (Thermo Fisher). THP-1 monocytes were treated with freshly prepared Phorbol 12-myristate 13-acetate (PMA, Sigma Aldrich) (50 ng/mL) supplemented RPMI-1640 media for 24 h to promote their differentiation into macrophage. Upon 24 h of PMA stimulation, almost all THP-1 cells become adherent.

To study macrophage response *in vitro*, THP-1 derived macrophages were trypsinized and seeded onto the hMSC/ECM or hMSC/EC/ECM constructs with seeding density of 10^5 cells/cm^2 to maintain macrophage to hMSC ratio 10:1 as suggested in a previously published study [36]. After seeding macrophage onto hMSC/ECM or hMSC/EC/ECM constructs, the co-cultures were maintained for another 7 days under physiological normoxia (21% O_2, 5% CO_2).

5.4. Evaluating macrophage-metabolism using fluorescence-life time (FLIM) imaging

Macrophages seeded onto anisotropic or isotropic hMSC-ECM as well as anisotropic or isotropic hMSC/EC/ECM were observed after 3 and 7 days by a custom-built multi-photon fluorescence lifetime microscope (Marianas, 3i). THP-1 derived macrophages co-cultured on hMSC/ECM or pre-vascularized ECM constructs were labeled as hMSC/macrophage or hMSC/EC/macrophage. A 40X water-immersion objective (1.1 NA) was used to couple the excitation and emitted light through an inverted microscope (ZEISS, Axio Observer 7). A tunable (680 nm–1080 nm) Ti: sapphire femtosecond laser (COHERENT, Chameleon Ultra II) was tuned to 750 nm with 12 mW for Nicotinamide adenine dinucleotide phosphate (NAD(P)H) excitation and 890 nm with 15 mW for Flavin adenine dinucleotide (FAD) stimulation. A 447/60 nm bandpass filter isolated NAD(P)H fluorescence and a 550/88 nm bandpass filter isolated FAD fluorescence. Fluorescence lifetime images were acquired using photomultiplier tube (PMT) detectors (HAMAMATSU) attached to time-correlated single photon counting (TCSPC) electronics (SPC- 150 N, Becker and Hickl). A pixel dwell time of 50 μs with 5 frame repeats was used, and each image of 256 × 256 pixels (270 μm × 270 μm) was obtained with an integration time of around 60 s. Both NAD(P)H and FAD images were acquired sequentially for five randomly selected positions for each sample, and three technical replicates were performed to ensure the reliability of the results. The instrument response function (IRF) was measured from the second harmonic signal generated from urea crystals excited at 900 nm and captured in the PMT of the NAD(P)H channel. The fluorescence lifetime measurements were validated by imaging YG fluorescent beads (Fluoresbrite YG beads, 20 mm, Polysciences). The beads were measured to have an average fluorescence lifetime of 2.1ns, which is consistent with published studies [70]. Fluorescence lifetime decays of NAD(P)H and FAD were deconvolved from the IRF and fit to a two-component exponential decay (SPCImage; Becker & Hickl) to quantify the lifetimes of free and protein-bound NAD(P)H and FAD [71,72]. A spatial bin of the center pixel and nine surrounding pixels was used. The fluorescence lifetime components of each pixel were computed by from a two-component exponential model, $I(t) = \alpha_1 e^{-t/\tau_1} + \alpha_2 e^{-t/\tau_2} + C$, where $I(t)$ is the fluorescence intensity at time t, α_1 and α_2 are the fractional contributions of the short and long lifetime components, respectively, τ_1 and τ_2 are their fluorescence lifetimes, and C accounts for background light. Images were then segmented into each cell based on the NAD(P)H intensity images by CellProlifer using a customized pipeline, and the mean values of the pixels in each cell region were calculated as the endpoints of each cell [73].

5.5. Reverse transcription-quantitative polymerase chain reaction (RT-qPCR)

RNA was extracted using RNeasy Mini Kit (Qiagen, Valencia, CA) and was treated with DNase I (Thermo Fisher) to remove genomic DNA contamination. Extracted RNA was reverse transcribed using VILO master mix (Thermo Fisher) and amplified by the QuantStudio3™ Real-Time PCR System (Applied Biosystems Waltham, MA) using SYBR green Real Time PCR Master Mixes (Life Technology) and commercially available primers (Sigma-Aldrich) (Table S1). GAPDH gene was used as an endogenous control and data were analyzed using the ΔΔCt method. Amplification measurements were performed in triplicate, and three individual samples were tested for statistical analysis.

5.6. Western blotting

The tissue lysate from hMSC/macrophage and hMSC/EC/macrophage were prepared in radioimmunoprecipitation assay (RIPA) buffer supplemented with EDTA-free Protease Inhibitor (Sigma Aldrich) and Halt™ Phosphatase Inhibitor Cocktail (Thermo Fisher Scientific) according to the manufacturer's instructions. Denatured cell lysates were separated by sodium dodecyl sulfate–polyacrylamide gel electrophoresis (SDS-PAGE) and transferred onto a polyvinylidene fluoride (PVDF) membrane. PVDF membranes were blocked using Intercept® (PBS) Blocking Buffer (LI-COR) followed by overnight incubation in primary antibody with 1:1000 dilution at 4 °C. The membranes were stained using IRDye® 800CW goat anti-rabbit and IRDye® 680LT goat anti-mouse secondary antibodies (LI-COR) with 1:5000 dilution for 1 h at room temperature (RT) and imaged with Odyssey® clx imaging system (LI-COR). For western blot analysis, technical triplicates (n = 3) were considered for each experimental group. Total protein from the technical triplicates were collectively quantified and loaded onto the gel to represent each experimental group.

5.7. Cytokine array analysis

The tissue lysate from hMSC/macrophage and hMSC/EC/macrophage groups were prepared in lysis buffer 17 (R&D systems) supplemented with 10 μg/mL Aprotinin (Tocris Bioscience, Ellisville, MO), 10 μg/mL Leupeptin (Tocris Bioscience) and 10 μg/mL Pepstatin (Tocris Bioscience). 100 μg of tissue lysates as well as 250 μl of conditioned media from Day 7 hMSC/MP and hMSC/EC/MP groups were analyzed using Proteome Profiler human XL cytokine array kit (ARY022B, R&D systems) following manufacturer's instructions. The membranes were stained using IRDye-800 CW streptavidin antibody (LI-COR) and imaged with Odyssey® clx imaging system (LI-COR). For cytokine array analysis, technical triplicates (n = 3) were considered for each experimental group. Total protein from the technical triplicates were collectively quantified and loaded onto a single cytokine array membrane to generate one membrane per experimental group.

5.8. Animal experiments

Animal experiments were performed following protocols approved by the institutional committee for animal use and care regulations at Michigan Technological University and Texas A&M University. Athymic *Foxn1*^{rnu}-Nude rats (male, 8 weeks old, 200–250 g weight) were purchased from Charles River Laboratories (Wilmington, MA). Rats were anesthetized with isoflurane and their backs were shaved with clippers. Each rat was surgically implanted with two constructs: (1) hMSC/ECM and (2) hMSC/EC/ECM, both with aligned architecture. A small incision was made on the right and left side of the rat to expose the subcutaneous space in which hMSC/ECM or hMSC/EC/ECM constructs were implanted respectively and were not sutured with host tissues. Both incisions were kept at least 2–3 cm apart from each other and closed with suture clips. The rats were euthanized on day 3, 7, 14 and 28 post implantation and the skin samples were harvested from the right side and the left side of the back that contained hMSC/ECM and hMSC/EC/ECM implants (as illustrated in Fig. 1). A region of skin from another random area from the back was also harvested to serve as a control (as illustrated in Fig. 1). Therefore, a total of 3 samples were harvested from an individual rat. A total of 20 rats were used in this study, among which 5 rats were sacrificed at each time point (n = 5). Before euthanization, rats were injected with 100 μl of biotinylated Ulex Europaeus Agglutinin I (UEA I) (Vector Labs, Burlingame, CA) in the left ventricle of heart to allow UEA-I to enter the circulation to detect the anastomosis of engineered vessels. The harvested samples were submerged in OCT compound and were immersed in liquid nitrogen. Samples were stored at −80 °C until

sectioning. Harvested tissue samples were sectioned at 6 μm thickness with the interval of ~50–100 μm using a cryostat (Thermo Fisher Scientific, HM 525NX). Tissue sections were placed on the Histobond slides (VWR International, Radnor, PA) and fixed with 4% paraformaldehyde prior to staining.

5.9. Immunofluorescence staining and histological analysis

Immunofluorescence (IF) staining was performed to label cellular and ECM components of prevascularized constructs using primary antibodies targeting the CD31 EC-specific marker, the CD68 macrophage specific marker, the F-actin cytoskeletal marker and the collagen-I and fibronectin hDF-ECM-specific markers. Secondary antibodies goat-anti mouse Alexa Fluor™ 488 conjugate and goat-anti rabbit Alexa Fluor™ 555 conjugate were used for IF staining. Cell nuclei were stained with 4′,6-diamidino-2-phenylindole, dihydrochloride (DAPI). Z-stacking in confocal imaging was performed to individually measure the thickness of hDF-ECM (base scaffold) as well as pre-vascularized layer (hMSC/EC-layer).

Tissue sections were stained in the hematoxylin and eosin (H&E) solutions (Sigma-Aldrich) as described previously [74], to observe the overall histology of implants over the period of 28 days. Anastomosis of engineered micro-vessels with host vasculature was determined by using streptavidin Alexa Fluor™ 488 Conjugate secondary antibody (Invitrogen) that specifically binds with biotinylated UEA-I lectin using IF staining. Besides lectin, engineered micro-vessels were also stained with polyclonal antibodies targeting endothelial markers CD31/PECAM-1. Implanted cells were observed via human nuclear antigen (hNA) staining. Recruitment of macrophage were observed via staining macrophage-specific marker CD68. Secondary antibodies goat-anti mouse Alexa Fluor™ 488 conjugate and goat-anti rabbit Alexa Fluor™ 555 conjugate were used for IF staining. Cell nuclei were stained with 4′, 6-diamidino-2-phenylindole, dihydrochloride (DAPI).

5.10. Statistical analysis

Statistical comparisons between experimental groups were performed in triplicated experiments by one-way ANOVA and Tukey's post hoc test using GraphPad Prism software. In FLIM based analysis, six non-overlapping images were captured from each experimental triplicate ($n = 3$). Each image contained between 150 and 300 macrophages. Fluorescence lifetime components of NAD(P)H and FAD for each of the macrophage were obtained. In FLIM based analysis, statistical comparisons between experimental groups were performed by two-sided t-tests with the Bonferroni correction for multiple comparisons using R Studio software. For *in vitro* image based analysis, six non-overlapping images were captured from each technical triplicate from each experimental group and analyzed. Images with size 2.336 mm^2 area (1760.00 μm × 1327.27 μm) were used for microvascular network characterization. For *in vivo* image based analysis, images with size 0.58 mm^2 (878.94 μm × 662.84 μm) were captured from 20 tissue-sections with 50–100 μm of interval from each skin sample were analyzed. Results are displayed as mean ± standard deviation and were considered statistically significant for $*p < 0.05$, $**p < 0.01$, $***p < 0.001$, $****p < 0.0001$.

Data and materials availability

All data are available in the main text or the supplementary materials.

Animal experiments

Animal experiments were performed following protocols approved by the institutional committee for animal use and care regulations at Michigan Technological University and Texas A&M University.

Funding

This study was supported by the National Institutes of Health 795 (R01HL146652) and the National Science Foundation (1703570) to FZ.

Declaration of competing interest

Authors declare that they have no competing interests.

CRediT authorship contribution statement

Dhavan Sharma: Conceptualization, Methodology, Writing – original draft, Writing – review & editing. **Archita Sharma:** Methodology. **Linghao Hu:** Methodology, Writing – original draft. **Te-An Chen:** Methodology. **Sarah Voon:** Methodology. **Kayla J. Bayless:** Writing – review & editing. **Jeremy Goldman:** Writing – review & editing. **Alex J. Walsh:** Writing – review & editing. **Feng Zhao:** Conceptualization, Supervision, Writing – review & editing.

Acknowledgements

We sincerely acknowledge Dr. Jonathan Bova and Dr. Weilue He for their help in the animal experiments. We also acknowledge Texas A&M University Microscopy and Imaging Center Core Facility (RRID: SCR_022128), and the Integrated Microscopy and Imaging Laboratory at Texas A&M College of Medicine (RRID:SCR_021637) for providing microscopy resources.

Appendix A. Supplementary data

Supplementary data to this article can be found online at https://doi.org/10.1016/j.bioactmat.2023.07.023.

References

[1] R.K. Jain, et al., Engineering vascularized tissue, Nat. Biotechnol. 23 (7) (2005) 821–823.
[2] E.R. Clark, E.L. Clark, Microscopic Observations on the Growth of Blood Capillaries in the Living Mammal, 64, 1939, pp. 251–301, 2.
[3] D. Sharma, et al., Upgrading prevascularization in tissue engineering: a review of strategies for promoting highly organized microvascular network formation, Acta Biomater. 95 (2019).
[4] F. Simunovic, G. Finkenzeller, Vascularization Strategies in Bone Tissue Engineering, 10, 2021, p. 1749, 7.
[5] P. Muangsanit, R.J. Shipley, J.B. Phillips, Vascularization Strategies for Peripheral Nerve Tissue Engineering, 301, 2018, pp. 1657–1667, 10.
[6] J. Paek, et al., Microphysiological engineering of self-assembled and perfusable microvascular beds for the production of vascularized three-dimensional human microtissues, ACS Nano 13 (7) (2019) 7627–7643.
[7] J. Kim, et al., Engineering of a biomimetic pericyte-covered 3D microvascular network, PLoS One 10 (7) (2015), e0133880.
[8] M.A. Winkelman, et al., Interstitial flow enhances the formation, connectivity, and function of 3D brain microvascular networks generated within a microfluidic device, Lab Chip 22 (1) (2022) 170–192.
[9] K.S. Lim, et al., Microchannels in development, survival, and vascularisation of tissue analogues for regenerative medicine, Trends Biotechnol. 37 (11) (2019) 1189–1201.
[10] M. Schwarz, et al., Optoacoustic dermoscopy of the human skin: tuning excitation energy for optimal detection bandwidth with fast and deep imaging in vivo, IEEE Trans. Med. Imag. 36 (6) (2017) 1287–1296.
[11] N. Kaneko, et al., Three-dimensional reconstruction of the human capillary network and the intramyocardial micronecrosis, Am. J. Physiol. Heart Circ. Physiol. 300 (3) (2011) H754–H761.
[12] D. Sharma, et al., Constructing biomimetic cardiac tissues: a review of scaffold materials for engineering cardiac patches, Emergent Materials 2 (2) (2019) 181–191.
[13] I.M. Olfert, et al., Advances and challenges in skeletal muscle angiogenesis, Am. J. Physiol. Heart Circ. Physiol. 310 (3) (2016) H326–H336.
[14] Z. Qian, et al., Engineering stem cell cardiac patch with microvascular features representative of native myocardium, Theranostics 9 (8) (2019) 2143–2157.
[15] L. Zhang, et al., Prevascularization of natural nanofibrous extracellular matrix for engineering completely biological three-dimensional prevascularized tissues for diverse applications, Journal of tissue engineering and regenerative medicine 12 (3) (2018) e1325–e1336.

[16] Y. Fujita, et al., Clinical application of mesenchymal stem cell-derived extracellular vesicle-based therapeutics for inflammatory lung diseases, J. Clin. Med. 7 (10) (2018).
[17] M.F. Pittenger, et al., Mesenchymal stem cell perspective: cell biology to clinical progress, npj Regenerative Medicine 4 (1) (2019) 22.
[18] D. Sharma, F. Zhao, Updates on clinical trials evaluating the regenerative potential of allogenic mesenchymal stem cells in COVID-19, npj Regenerative Medicine 6 (1) (2021) 37.
[19] Q. Xing, et al., Highly aligned nanofibrous scaffold derived from decellularized human fibroblasts, Adv. Funct. Mater. 24 (20) (2014) 3027–3035.
[20] L. Zhang, et al., Prevascularization of natural nanofibrous extracellular matrix for engineering completely biological three-dimensional prevascularized tissues for diverse applications, J Tissue Eng Regen Med 12 (3) (2018) e1325–e1336.
[21] A.I. Caplan, Mesenchymal stem cells: time to change the name!, Stem Cells Transl Med 6 (6) (2017) 1445–1451.
[22] D. Sharma, J. Chica, F. Zhao, Mesenchymal Stem Cells for Pre-vascularization of Engineered Tissues, 2018.
[23] B. Rolstad, The athymic nude rat: an animal experimental model to reveal novel aspects of innate immune responses? Immunol. Rev. 184 (2001) 136–144.
[24] M.J. McClure, et al., RNU (Foxn1RNU-Nude) Rats Demonstrate an Improved Ability to Regenerate Muscle in a Volumetric Muscle Injury Compared to Sprague Dawley Rats 8 (1) (2021) 12.
[25] Adipose-Derived Stem Cells Promote Angiogenesis and Tissue Formation for in Vivo Tissue Engineering 19 (2013) 1327–1335, 11-12.
[26] H. Nakagawa, et al., Human Mesenchymal Stem Cells Successfully Improve Skin-Substitute Wound Healing, 153, 2005, pp. 29–36, 1.
[27] Human Umbilical Vein Endothelial Cell Support Bone Formation of Adipose-Derived Stem Cell-Loaded and 3D-Printed Osteogenic Matrices in the Arteriovenous Loop Model 27 (2021) 413–423, 5-6.
[28] A. Theodossiou, et al., Autofluorescence imaging to evaluate cellular metabolism, J. Vis. Exp. (2021), https://doi.org/10.3791/63282.
[29] A.J. Walsh, et al., Classification of T-cell activation via autofluorescence lifetime imaging, Nat Biomed Eng 5 (1) (2021) 77–88.
[30] Melissa C. Skala, et al., In Vivo Multiphoton Microscopy of NADH and FAD Redox States, Fluorescence Lifetimes, and Cellular Morphology in Precancerous Epithelia. PNAS, 2007.
[31] C. Stringari, et al., Phasor approach to fluorescence lifetime microscopy distinguishes different metabolic states of germ cells in a live tissue, Proc. Natl. Acad. Sci. U. S. A. 108 (33) (2011) 13582–13587.
[32] J.R. Lakowicz, Principles of Fluorescence Spectroscopy, MD 21201, Springer US, University of Maryland School of Medicine, Baltimore, 2006.
[33] L. JR, et al., Fluorescence lifetime imaging of free and protein-bound NADH, Proc. Natl. Acad. Sci. U.S.A. 89 (4) (1992) 1271–1275.
[34] K. Drozdowicz-Tomsia, et al., Multiphoton fluorescence lifetime imaging microscopy reveals free-to-bound NADH ratio changes associated with metabolic inhibition, J. Biomed. Opt. 19 (8) (2014), 086016.
[35] J.T. Sharick, et al., Protein-bound NAD(P)H lifetime is sensitive to multiple fates of glucose carbon, Sci. Rep. 8 (1) (2018) 5456.
[36] A.B. Vasandan, et al., Human Mesenchymal stem cells program macrophage plasticity by altering their metabolic status via a PGE2-dependent mechanism, Sci. Rep. 6 (1) (2016), 38308.
[37] A. Dorronsoro, et al., Intracellular role of IL-6 in mesenchymal stromal cell immunosuppression and proliferation, Sci. Rep. 10 (1) (2020), 21853.
[38] H.-X. Wei, B. Wang, B. Li, IL-10 and IL-22 in Mucosal Immunity: Driving Protection and Pathology, 2020, p. 11.
[39] W.G. Chang, L.E. Niklason, A short discourse on vascular tissue engineering, npj Regenerative Medicine 2 (1) (2017) 7.
[40] X. Chen, et al., Rapid anastomosis of endothelial progenitor cell-derived vessels with host vasculature is promoted by a high density of cotransplanted fibroblasts, Tissue Eng. 16 (2) (2010) 585–594.
[41] J.D. Baranski, et al., Geometric control of vascular networks to enhance engineered tissue integration and function, Proc. Natl. Acad. Sci. U. S. A. 110 (19) (2013) 7586–7591.
[42] M.A. Redd, et al., Patterned human microvascular grafts enable rapid vascularization and increase perfusion in infarcted rat hearts, Nat. Commun. 10 (1) (2019) 584.
[43] K.L. Coulombe, C.E. Murry, Vascular perfusion of implanted human engineered cardiac tissue, Proc. IEEE Annu. NE Bioeng. Conf. 2014 (2014).
[44] E.M. Renkin, C. Crone, Microcirculation and capillary exchange, in: R. Greger, U. Windhorst (Eds.), Comprehensive Human Physiology: from Cellular Mechanisms to Integration, Springer Berlin Heidelberg, Berlin, Heidelberg, 1996, pp. 1965–1979.
[45] S. Galvan-Pena, L.A. O'Neill, Metabolic reprograming in macrophage polarization, Front. Immunol. 5 (2014) 420.
[46] E.J. Hoffmann, S.M. Ponik, Biomechanical contributions to macrophage activation in the tumor microenvironment, Front. Oncol. 10 (2020) 787.
[47] A. Alfonso-Garcia, et al., Label-free identification of macrophage phenotype by fluorescence lifetime imaging microscopy, J. Biomed. Opt. 21 (4) (2016), 46005.
[48] T.M. Heaster, et al., Autofluorescence imaging of 3D tumor-macrophage microscale cultures resolves spatial and temporal dynamics of macrophage metabolism, Cancer Res. 80 (23) (2020) 5408–5423.
[49] I. Georgakoudi, K.P. Quinn, Optical imaging using endogenous contrast to assess metabolic state, Annu. Rev. Biomed. Eng. 14 (2012) 351–367.
[50] J. Liao, D.C. Hargreaves, The alternative macrophage relay: STAT6 passes the baton to EGR2, Genes Dev. 34 (21–22) (2020) 1407–1409.
[51] B. Daniel, et al., The transcription factor EGR2 is the molecular linchpin connecting STAT6 activation to the late, stable epigenomic program of alternative macrophage polarization, Genes Dev. 34 (21–22) (2020) 1474–1492.
[52] S.P. Arlauckas, et al., Arg1 expression defines immunosuppressive subsets of tumor-associated macrophages, Theranostics 8 (21) (2018) 5842–5854.
[53] Z. Yang, X.-F. Ming, Functions of arginase isoforms in macrophage inflammatory responses: impact on cardiovascular diseases and metabolic disorders, Front. Immunol. 5 (2014) 533, 533.
[54] W. Jiang, J. Xu, Immune modulation by mesenchymal stem cells, Cell Prolif. 53 (1) (2020), e12712.
[55] G. Arango Duque, A. Descoteaux, Macrophage Cytokines: Involvement in Immunity and Infectious Diseases, 5, 2014.
[56] A. Zlibut, I.C. Bocsan, L. Agoston-Coldea, Chapter five - pentraxin-3 and endothelial dysfunction, in: G.S. Makowski (Ed.), Advances in Clinical Chemistry, Elsevier, 2019, pp. 163–179.
[57] J. Sheng, Z. Xu, Three decades of research on angiogenin: a review and perspective, Acta Biochim. Biophys. Sin. 48 (5) (2015) 399–410.
[58] N. Mahmood, C. Mihalcioiu, S.A. Rabbani, Multifaceted Role of the Urokinase-type Plasminogen Activator (uPA) and its Receptor (uPAR): Diagnostic, Prognostic, and Therapeutic Applications, 8, 2018.
[59] J.M. Cash, et al., Genetic mapping of the athymic nude (RNU) locus in the rat to a region on Chromosome 10, Mamm. Genome 4 (1) (1993) 37–42.
[60] M.J. McClure, et al., RNU (Foxn1 (RNU)-Nude) rats demonstrate an improved ability to regenerate muscle in a volumetric muscle injury compared to sprague dawley rats, Bioengineering 8 (1) (2021).
[61] P.L. Graney, et al., Macrophages of diverse phenotypes drive vascularization of engineered tissues, Sci. Adv. 6 (18) (2020) eaay6391.
[62] R.Z. Lin, et al., Host non-inflammatory neutrophils mediate the engraftment of bioengineered vascular networks, Nat Biomed Eng 1 (2017).
[63] W. Song, et al., Engineering transferrable microvascular meshes for subcutaneous islet transplantation, Nat. Commun. 10 (1) (2019) 4602.
[64] T. Deuse, et al., Hypoimmunogenic derivatives of induced pluripotent stem cells evade immune rejection in fully immunocompetent allogeneic recipients, Nat. Biotechnol. 37 (3) (2019) 252–258.
[65] C. Song, et al., Generation of individualized immunocompatible endothelial cells from HLA-I-matched human pluripotent stem cells, Stem Cell Res. Ther. 13 (1) (2022) 48.
[66] H. Choi, et al., Anti-inflammatory protein TSG-6 secreted by activated MSCs attenuates zymosan-induced mouse peritonitis by decreasing TLR2/NF-κB signaling in resident macrophages, Blood 118 (2) (2011) 330–338.
[67] A.I. Caplan, et al., Optimizing mesenchymal stem cell-based therapeutics, Curr. Opin. Biotechnol. 20 (5) (2009) 531–536.
[68] D. Sharma, et al., Polydopamine and collagen coated micro-grated polydimethylsiloxane for human mesenchymal stem cell culture, Bioact. Mater. 4 (2019) 142–150.
[69] D. Sharma, M. Ferguson, F. Zhao, Chapter 1 - a step-by-step protocol for generating human fibroblast cell-derived completely biological extracellular matrix scaffolds, in: D. Caballero, S.C. Kundu, R.L. Reis (Eds.), Methods in Cell Biology, Academic Press, 2020, pp. 3–13.
[70] D.K. Bird, et al., Metabolic mapping of MCF10A human breast cells via multiphoton fluorescence lifetime imaging of the coenzyme NADH, Cancer Res. 65 (19) (2005) 8766–8773.
[71] J.R. Lakowicz, et al., Fluorescence lifetime imaging of free and protein-bound NADH, Proc. Natl. Acad. Sci. U. S. A. 89 (4) (1992) 1271–1275.
[72] N. Nakashima, et al., Picosecond fluorescence lifetime of the coenzyme of D-amino acid oxidase, J. Biol. Chem. 255 (11) (1980) 5261–5263.
[73] A.J. Walsh, M.C. Skala, An automated image processing routine for segmentation of cell cytoplasms in high-resolution autofluorescence images, in: Proc. SPIE 8948, Multiphoton Microscopy in the Biomedical Sciences XIV, 2014, p. 89481M.
[74] W. Jia, et al., Preservation of Microvascular Integrity and Immunomodulatory Property of Prevascularized Human Mesenchymal Stem Cell Sheets, 15, 2021, pp. 207–218, 3.